

Diverse Jet Structures Consistent with the Off-axis Afterglow of GRB 170817A

Kazuya Takahashi¹[★] and Kunihito Ioka¹

¹Center for Gravitational Physics, Yukawa Institute for Theoretical Physics, Kyoto University, Kyoto, 606-8502, Japan

Accepted XXX. Received YYY; in original form ZZZ

ABSTRACT

The jet structure of short gamma-ray bursts (GRBs) has been controversial after the detection of GRB 170817A as the electromagnetic counterparts to the gravitational wave event GW170817. Different authors use different jet structures for calculating the afterglow light curves. We formulated a method to inversely reconstruct the jet structure uniquely from a given off-axis GRB afterglow, without assuming any functional form of the structure. By systematically applying our inversion method, we find that more diverse jet structures are consistent with the observed afterglow of GRB 170817A within errors: such as hollow-cone, spindle, Gaussian, and power-law jet structures. In addition, the total energy of the reconstructed jet is arbitrary, proportional to the ambient density n_0 , with keeping the same jet shape if the parameters satisfy the degeneracy combination $n_0 \varepsilon_B^{(p+1)/(p+5)} \varepsilon_e^{4(p-1)/(p+5)} = \text{const.}$. Observational accuracy less than ~ 6 per cent is necessary to distinguish the different shapes, while the degeneracy of the energy scaling would be broken by observing the spectral breaks. Future events in denser environment with brighter afterglows and observable spectral breaks are ideal for our inversion method to pin down the jet structure, providing the key to the jet formation and propagation.

Key words: gamma-ray bursts – methods: analytical

1 INTRODUCTION

The gravitational wave event GW170817 with the detection of electromagnetic counterparts, in particular GRB 170817A and its afterglow, has revealed that a coalescence of two neutron stars leads to a short gamma-ray burst (GRB). The successful launch and propagation of a relativistic jet is supported by the superluminal motion of the compact radio source (Mooley et al. 2018b; Ghirlanda et al. 2019) and the rapid decline of the afterglow light curve after the peak (Mooley et al. 2018a,c; Lamb et al. 2019; Makhathini et al. 2020). The gamma-ray emission is apparently faint because the jet is off-axis, misaligned with the line of sight (Abbott et al. 2017c; Ioka & Nakamura 2018, 2019, and references therein). In order for the jet to break out the merger ejecta, the jet power should be similar to the other short GRBs (Nagakura et al. 2014; Hamidani et al. 2019).

GRB 170817A also revealed that the jet has to be structured with an angular dependent energy distribution, which is required to explain the slowly rising light curves of the afterglow (Mooley et al. 2018a). However, the exact jet structure is still controversial. Different authors assume different structures for calculating the afterglow light curves. Often

used structure is a Gaussian (Zhang & Mészáros 2002; Rossi et al. 2004; Lyman et al. 2018; Resmi et al. 2018; Troja et al. 2019; Lamb & Kobayashi 2018; Lamb et al. 2019; Gill & Granot 2020; Ryan et al. 2020; Troja et al. 2020) or a power law (Mészáros et al. 1998; Rossi et al. 2002, 2004; Zhang & Mészáros 2002; Granot & Kumar 2003; Lamb & Kobayashi 2018; D’Avanzo et al. 2018; Ghirlanda et al. 2019; Beniamini et al. 2020; Gill & Granot 2020; Ryan et al. 2020), although there is no strong motivation to limit the jet structure to these specific forms. The jet structure is crucial to off-axis gamma-ray emission (Beniamini et al. 2019; Ioka & Nakamura 2019). Furthermore, the jet structure is potentially a clue to the jet launching, collimation, and propagation processes as inferred from numerical simulations (Aloy et al. 2005; Nagakura et al. 2014; Duffell et al. 2015; Lazzati et al. 2017; Murguia-Berthier et al. 2017; Kathirgamaraju et al. 2018, 2019; Xie 2018; Geng et al. 2019; Gill et al. 2019; Gottlieb et al. 2020; Nathanail et al. 2020).

We recently discovered that a hollow-cone jet structure is also a candidate for GRB 170817A for the first time (Takahashi & Ioka 2020, hereafter TI20). It was discovered by a new approach that inversely reconstructs a jet structure from a given afterglow light curve in off-axis GRBs. One of the advantages of the method is that it does not prefix a functional form of the jet structure. Thus, as demonstrated

[★] E-mail: kazuya.takahashi@yukawa.kyoto-u.ac.jp

by the discovery of a hollow-cone jet, the method can reconstruct a non-trivial jet structure that is different from a Gaussian jet or a power-law one. Another advantage is that the method uniquely determines a jet structure for a given light curve, once the other model parameters are fixed. The hollow-cone jet is reconstructed from a straight-line light curve, which is the simplest example that fits the rising slope of the observed afterglow. In addition, the hollow-cone type structure is always reconstructed by using the straight-line light curve, irrespective of the other model parameters such as the viewing angle and the jet edge structure while the jet structure changes quantitatively. This result indicates that the light curve shape is the paramount feature for determining the jet structure. However, in reality, we could draw another light curve to fit the observed data within the uncertainty, which leads to a Gaussian jet or a power-law one depending on the light curve shape. So far, it has not been studied thoroughly how the jet structure changes for different light curves.

This paper searches for jet structures that are consistent with the afterglow of GRB 170817A in a systematic way. We apply the inversion method in [TI20](#) to more general types of the light curves by taking into account the curvature of the light curve. The light curve shape is changed in a parametric way so that it is consistent with the afterglow of GRB 170817A. We find that a little difference of the light curve creates a large diversity of non-trivial jet structures. We also find that the total energy of the jet is not determined because we can change the total energy without changing the jet shape by appropriately tuning the afterglow parameters.

The paper is organized as follows. In [Section 2](#), we introduce the parametric light curve and other model parameters used in this study after briefly summarizing the inversion method in [TI20](#). Then, the various jet structures reconstructed from the generic light curves are presented in [Section 3](#). We discuss the reason of the diversity of the jet candidates in [Section 4](#). Finally, we make a conclusion on the jet structure of GRB 170817A in [Section 5](#). Throughout the paper, we attach a prime to the quantities evaluated in the fluid rest frame.

2 METHOD

2.1 Brief Review of the Inversion Method

We consider an axi-symmetric relativistic jet propagating into the interstellar medium with a constant number density n_0 . The jet energy has an angular structure $E(\theta)$, where E is the isotropic equivalent energy and θ is the polar angle measured from the jet axis. A shock is formed in the interstellar medium, and is well described by a self-similar solution of [Blandford & McKee \(1976\)](#) as if it were a portion of a spherical blast wave until the shock is further decelerated to non-relativistic speeds ([Kumar & Granot 2003](#); [Zhang & MacFadyen 2009](#); [van Eerten & MacFadyen 2012](#)). The afterglow is produced by synchrotron radiation emitted from electrons accelerated to a power-law energy distribution with a spectral index p at the shock with a magnetic field in the downstream ([Sari et al. 1998](#)). The shocked region is approximated by a thin shell ([van Eerten et al. 2010](#)).

Then, we can calculate the afterglow light curve for a given jet energy structure $E(\theta)$.

Inversely, we can reconstruct the jet structure $E(\theta)$ from a given afterglow light curve in the case of off-axis GRBs. This is possible because the jet structure gradually becomes visible from the jet edge to the central region, as the relativistic beaming angle increases due to the deceleration of the jet sweeping the ambient material. The emission centroid gradually moves from the jet edge region close to the observer direction toward the jet axis, scanning the jet structure as time passes and reflecting the jet structure into the light curve.

Based on the above idea, we recently formulated an inversion method that reconstructs a jet structure from an afterglow light curve ([TI20](#)). While the observed light curve is calculated by integrating the synchrotron emission radiated from the shock surface, we reverse the integral into an ordinary differential equation for $E(\theta)$ in [Equation \(1\)](#) below. By integrating [Equation \(1\)](#), the jet structure is uniquely determined from a given afterglow light curve. Since the scan of the jet surface is finished when the emission site reaches the jet axis, the reconstruction method uses only a part of the rising portion of the light curve before the peak.

The inversion formula is given by (See [Appendix A](#) for a short review of the derivation and the detail)

$$\frac{d \ln E}{d \Theta} = \frac{8}{\theta_v - \Theta} - \frac{3K(T, \Theta, E(\Theta))}{F_\nu(T)} \left[\frac{d \log F_\nu}{d \log T}(T) - \frac{T}{F_\nu(T)} \int_0^{\theta_j} d\theta \frac{dK}{dT}(T, \theta, E(\theta)) \right]^{-1}, \quad (1)$$

where $F_\nu(T)$ is the observed flux with ν and T being the observed frequency and observer time, respectively. θ_v is the viewing angle measured from the jet axis. $\Theta(T)$ approximately corresponds to the polar angle of the emission centroid and satisfies [Equation \(A2\)](#). K is a function defined by [Equation \(A5\)](#), and θ_j is the jet truncation angle. A jet structure is obtained by integrating [Equation \(1\)](#) from $\Theta = \Theta(T_0)$ to $\Theta = 0$ for a given initial observer time T_0 . The effect of the cosmological redshift is neglected for simplicity. Necessary ingredients are the following:

(i) The rising portion of the light curve $F_\nu(T)$ ($T_0 \leq T \leq T_f$) for a given observed frequency ν . Here, T_0 is a given initial time. T_f is the time when $\Theta(T)$ reaches the jet axis and the reconstruction is completed, which depends on the jet structure and, hence, is not *a priori* known.

(ii) Model parameters $\{n_0, \epsilon_B, \epsilon_e, \theta_v, p, D\}$, where n_0 is the number density of the ambient interstellar medium, ϵ_B the energy conversion fraction from the shocked matter to the magnetic field, ϵ_e the energy conversion fraction from the shocked matter to the accelerated electrons, θ_v the viewing angle, p the energy spectral index of the accelerated electrons, and D the luminosity distance to the source.

(iii) Jet edge structure $E(\theta)$ for $\Theta(T_0) \leq \theta \leq \theta_j$ with θ_j being a jet truncation angle. This is given as a boundary condition for integrating [Equation \(1\)](#). The jet edge structure cannot be constrained from the light curve after T_0 in principle, since this region has been already scanned before T_0 .

This paper explores the allowed range of the jet structure by focusing on the uncertainty of the light curve listed

as (i) above. The observed data points generally include error bars and distribute sparsely in time. In the case of GRB 170817A, the rising slope could be fitted by a single power law $F_\nu \propto T^\alpha$ with α being a constant, while the slope may have a curvature. [TI20](#) used a simple power-law light curve, $d \log F_\nu / d \log T = 1.22 = \text{const.}$, and found that it always reconstructs qualitatively the same hollow-cone jet structure irrespective of the other parameters. Hence, it is a natural extension to consider more general light curves. The light curve used in this paper is given in Section 2.2.

In the rest of this subsection, we comment on the uncertainty of the other factors listed in (ii) and (iii) above. As mentioned later in Section 2.3, some of the model parameters listed in (ii) are degenerate and only a few are constrained from observations in general. In the case of GRB 170817A, the spectral index $p \sim 2.17$ ([Fong et al. 2019](#); [Troja et al. 2019](#)) and luminosity distance $D \sim 41$ Mpc ([Hjorth et al. 2017](#); [Cantiello et al. 2018](#)) are relatively well constrained while the others are not: The viewing angle θ_v is constrained from the detection of a super-luminal motion of a compact radio source in the afterglow phase ($14^\circ \lesssim \theta_v \lesssim 28^\circ$; [Mooley et al. 2018b](#)). Note that the uncertainty of the viewing angle leads to the uncertainty of the jet core width, θ_c . We reconstruct a wider jet structure if we assume a larger θ_v ([TI20](#)). This is because only the ratio of θ_v/θ_c is constrained from the rising part of afterglow light curves ([Nakar & Piran 2020](#)). n_0 is constrained in several ways: The diffuse X-ray emission from the host galaxy puts a constraint of $n_0 \leq 9.6 \times 10^{-3} \text{ cm}^{-3}$ ([Hajela et al. 2019](#)) while the non-detection of neutral hydrogen from the host also gives a looser upper limit $n_0 \leq 4 \times 10^{-2} \text{ cm}^{-3}$ ([Hallinan et al. 2017](#)). On the other hand, a cosmological simulation infers a lower limit of $n_0 \geq 2 \times 10^{-5} \text{ cm}^{-3}$ ([Shull et al. 2012](#); [Mooley et al. 2018a](#)). ϵ_B and ϵ_e have not been constrained from the observations so far, whereas $\epsilon_e = 0.1$ is a typical value in observations of other GRBs ([Kumar & Zhang 2015](#)) and in particle-in-cell simulations ([Sironi & Spitkovsky 2011](#)).

As noted in (iii), the jet edge structure is not constrained in principle from afterglow observations. However, the jet edge structure would be less important for the reconstruction of the inner part close to the jet axis, since the light curve for later time is dominated by the emission from the inner part. As shown in [TI20](#), the inner jet structure is qualitatively determined irrespective of whether the assumed edge structure is a Gaussian or a power-law. Especially, the jet truncation angle θ_j does not change the results qualitatively nor quantitatively as long as we choose a sufficiently large value ([TI20](#)).

2.2 Parametric Light Curve and Fiducial Setting

In the previous paper ([TI20](#)), we simplified the rising phase of the afterglow of GRB 170817A as a light curve with a constant slope (that is, the logarithmic derivative $d \log F_\nu / d \log T$ is constant). In this paper, we use more general light curves for the rising phase of the afterglow.

As a generalization, we consider the light curves that are parametrically given by

$$F_\nu(T) = F_0 \left(\frac{T}{T_0} \right)^{-aT_0+b} \exp[a(T - T_0)] \quad (T_0 \leq T \leq T_f), \quad (2)$$

where a is the curvature parameter, which controls the

changing rate of the light curve slope, and b is the initial slope as seen below. T_0 is the initial observer time and $F_0 = F_\nu(T_0)$ is the corresponding initial flux. The slope of the light curve in Equation (2) is

$$\frac{d \log F_\nu}{d \log T} = a(T - T_0) + b. \quad (3)$$

Thus, the light curve slope is initially given by $d \log F_\nu / d \log T = b$ at $T = T_0$ while it changes as time passes with a rate of a : In $(\log F_\nu, \log T)$ plane, $a > 0$ gives convex downward light curves, $a < 0$ gives convex upward ones, and $a = 0$ gives straight ones. We note that the case with $a = 0$ and $b = 1.22$ was investigated in [TI20](#), where a hollow-cone jet is inversely reconstructed.

Changing the curvature parameter a , we reconstruct the jet structure while we fix $\nu = 5.5$ GHz, $b = 1.22$, $T_0 = 9$ d, and $F_0 = 5.45 \mu\text{Jy}$ in Equation (2). We use the fiducial model parameters as $\epsilon_e = 0.1$, $p = 2.17$, $\theta_v = 0.387 \sim 22.2^\circ$, and $D = 41$ Mpc, while we treat n_0 and ϵ_B as free parameters to adjust the peak time and peak flux of the light curve that is forwardly calculated by the reconstructed jet. Note here that, since the jet structure is reconstructed from the rising portion of the light curve with $T_0 \leq T \leq T_f$ before the peak, we check as a post process whether the light curve forwardly calculated from the reconstructed jet agrees with the observations for $T > T_f$. We repeat the reconstruction procedure by iteratively tuning n_0 and ϵ_B until the forwardly calculated light curve matches the observed one. For the sake of quantitative accuracy, we use a more accurate afterglow equation, equation (18) in [TI20](#), to forwardly calculate the light curves than Equation (A1), which is equivalent to the inversion formula, Equation (1). The accurate afterglow equation takes into account the flux contribution from the entire jet surface, a smooth transition of the shock dynamics from the Blandford-McKee solution to the Sedov-Taylor solution ([Taylor 1950](#); [Sedov 1959](#); [van Eerten et al. 2010](#)), the spectral breaks at the characteristic and cooling frequencies (ν'_m and ν'_c , respectively; [Sari et al. 1998](#)), and so on. The relative difference between the light curves calculated by the accurate equation and Equation (A1) is within 5 per cent.¹

We assume the jet edge structure described by a Gaussian shape, which is given by

$$E(\theta) = E_0 \exp\left(-\frac{\theta^2}{2\theta_c^2}\right) \quad (\Theta(T_0) \leq \theta \leq \theta_j), \quad (4)$$

where we use $\theta_j = 0.61 \sim 35.0^\circ$ as our fiducial value although the choice of θ_j does not affect the results as long as it is large enough as mentioned in Section 2.1. We also note that the inner jet structure does not change qualitatively with the choice of the edge shape as noted before. E_0 , θ_c , and $\Theta(T_0)$ are self-consistently determined so that the edge structure becomes consistent with given $F_\nu(T_0)$ and $dF_\nu/dT(T_0)$ for each light curve (See Appendix B).

¹ The discrepancy between the light curves calculated by the accurate equation and Equation (A1) in this paper is mainly attributed to the inner cutoff angle $\Theta(T)$ in Equation (A1), which ignores the emission from the region near to the jet axis, $0 \leq \theta < \Theta(T)$. This discrepancy is inevitable, since $\Theta(T)$ plays an essential role in the inversion method. However, we can reduce it, if necessary, by using larger f_b in Equation (A2), which gives smaller $\Theta(T)$ for a fixed T (See [TI20](#) for details).

2.3 Degeneracy Relation in $(n_0, \varepsilon_B, \varepsilon_e)$

In the inversion process for a given light curve, we generally find that the jet structures with the same shape are reconstructed from different combinations of $(n_0, \varepsilon_B, \varepsilon_e)$. Here, we mean by the same shape that the jet structures have the same angle dependence, $f(\theta)$, except for the normalization, E_{axis} , as

$$E(\theta) = E_{\text{axis}} f(\theta) \quad (5)$$

with $f(0) = 1$ and $E_{\text{axis}} = E(0)$.

As shown in Appendix C, the degenerate combinations of $(n_0, \varepsilon_B, \varepsilon_e)$ are given by the following equation

$$\log n_0 + \frac{p+1}{p+5} \log \varepsilon_B + \frac{4(p-1)}{p+5} \log \varepsilon_e = \text{const.} =: \log \xi, \quad (6)$$

where ξ is the degeneracy parameter that characterizes the combination. For the degenerate combinations of $(n_0, \varepsilon_B, \varepsilon_e)$, which satisfy Equation (6) for a given ξ , the reconstructed jet structures have the same shape $f(\theta)$ while the energy E_{axis} is scaled by n_0 :

$$E_{\text{axis}} \propto n_0. \quad (7)$$

In this case, the total energy of the (one-sided) jet E_{tot} is also scaled as $E_{\text{tot}} \propto E_{\text{axis}} \propto n_0$, where E_{tot} is given by

$$E_{\text{tot}} = 2\pi \int_0^{\theta_j} E(\theta) \sin \theta d\theta = 2\pi E_{\text{axis}} \int_0^{\theta_j} f(\theta) \sin \theta d\theta \propto n_0. \quad (8)$$

By using Equations (6) and (8), we can rescale the total energy of a jet to a desired value without changing the afterglow light curve. For example, suppose that we have a jet structure with a total energy E_{tot} that is reconstructed from a light curve with a parameter set $(n_0, \varepsilon_B, \varepsilon_e)$. Then, if we change the total energy to a desired value \tilde{E}_{tot} , the corresponding number density \tilde{n}_0 is given by Equation (8) as follows:

$$\tilde{n}_0 = \frac{\tilde{E}_{\text{tot}}}{E_{\text{tot}}} n_0. \quad (9)$$

According to Equations (6) and (9), the appropriate combinations of the microphysical parameters, $(\tilde{\varepsilon}_B, \tilde{\varepsilon}_e)$, should satisfy

$$\tilde{\varepsilon}_B \tilde{\varepsilon}_e^{4(p-1)/(p+1)} = \varepsilon_B \varepsilon_e^{4(p-1)/(p+1)} \left(\frac{\tilde{E}_{\text{tot}}}{E_{\text{tot}}} \right)^{(p+5)/(p+1)}. \quad (10)$$

3 RESULTS

We reconstruct the jet structures by systematically changing the light curve slope. We use the light curve given by Equation (2) and control the slope by changing the curvature parameter a . We determine the ambient number density n_0 and microphysical parameter ε_B by adjusting the peak of the light curve that is forwardly calculated by the reconstructed jet while the other parameters are fixed to the fiducial values mentioned in Section 2.2.

In the first part, we discover various non-trivial jet structures that are consistent with GRB 170817A within the observational errors. The totally different structures are found to produce very similar light curves. In the second part, we demonstrate that the total energy can be altered without changing the structural shape nor the light curve by appropriately choosing a pair of (n_0, ε_B) .

Table 1. Parameters and results for Figure 1, where $a_{-3} = a/(10^{-3} \text{ d}^{-1})$ and $Q_x = Q/10^x$ in cgs units for the other quantities. a : the curvature parameter of the light curve in Equation (2). n_0 : the number density of the ambient matter. ε_B : the energy conversion fraction from the shocked matter to the magnetic field. ξ : the degeneracy parameter in Equation (6). E_0 and θ_c : the normalization and standard deviation of the Gaussian edge structure in Equation (4), respectively. E_{tot} : the total energy of the (one-sided) jet given by Equation (8).

a_{-3}	$n_{0,-3}$	$\varepsilon_{B,-4}$	ξ_{-6}	$E_{0,52}$	$\theta_{c,-2}$	$E_{\text{tot},50}$
-10	1.00	6.60	8.73	0.34	5.83	1.12
-8	1.00	4.41	7.31	0.56	5.86	1.60
-6	1.00	2.87	6.04	0.94	5.89	2.26
-4	1.00	1.85	4.98	1.64	5.91	3.08
-2	1.00	1.17	4.06	2.96	5.92	4.18
0	1.00	0.71	3.26	5.70	5.92	5.80
2	1.00	0.41	2.56	11.8	5.92	8.19

Table 2. Same as Table 1 but for Figure 3. The pair of (n_0, ε_B) for each model is chosen so that it gives $E_{0,52} = 2.51$ and the same ξ as in Table 1. $E_{\text{tot},50}/n_{0,-3}$ in the rightmost column is to coincide with $E_{\text{tot},50}$ in Table 1.

a_{-3}	$n_{0,-3}$	$\varepsilon_{B,-4}$	ξ_{-6}	$E_{0,52}$	$\theta_{c,-2}$	$E_{\text{tot},50}$	$\frac{E_{\text{tot},50}}{n_{0,-3}}$
-10	7.35	0.073	8.73	2.51	5.83	8.25	1.12
-8	4.52	0.15	7.31	2.51	5.86	7.26	1.60
-6	2.66	0.31	6.04	2.51	5.89	6.02	2.26
-4	1.53	0.70	4.98	2.51	5.91	4.72	3.08
-2	0.85	1.69	4.06	2.51	5.92	3.55	4.18
0	0.44	4.53	3.26	2.51	5.92	2.55	5.80
2	0.21	13.8	2.56	2.51	5.92	1.74	8.19

3.1 Various Non-trivial Jet Structures

We here use the light curves with the curvature parameter a in the range of $-10 \leq a/(10^{-3} \text{ d}^{-1}) \leq 2$. We fix $n_0 = 10^{-3} \text{ cm}^{-3}$ and tune ε_B for each light curve to adjust the peak. Figure 1 shows the results, with ε_B in Table 1 and also in Figure 2 (star-shaped points).

The left panel of Figure 1 shows the reconstructed jet structures. As a increases, the reconstructed jet structure continuously changes from a spindle type ($a \lesssim -6 \times 10^{-3} \text{ d}^{-1}$) to a hollow-cone type ($a \gtrsim -6 \times 10^{-3} \text{ d}^{-1}$) by passing through a Gaussian-like structure ($a \sim -6 \times 10^{-3} \text{ d}^{-1}$). For reference, we also depict a Gaussian jet in the left panel of Figure 1 (black dotted line). The standard deviations of the Gaussian edge are nearly the same among the models, $\theta_c \sim 5.9 \times 10^{-2}$, while the normalization, E_0 , is different among the models as listed in Table 1. The total energy E_{tot} , which is defined by Equation (8), increases for larger a as in Table 1.

In spite of the difference of the jet structures, they generate almost similar light curves, which are consistent with the observations as shown in the top right panel of Figure 1. We compare these light curves quantitatively with the Gaussian jet case (dotted lines). The black dotted line in the top right panel shows the light curve for the Gaussian jet, which is produced with $\varepsilon_B = 2.44 \times 10^{-4}$ while the other parameter values are the same as for the other models. The bottom right panel shows the relative difference

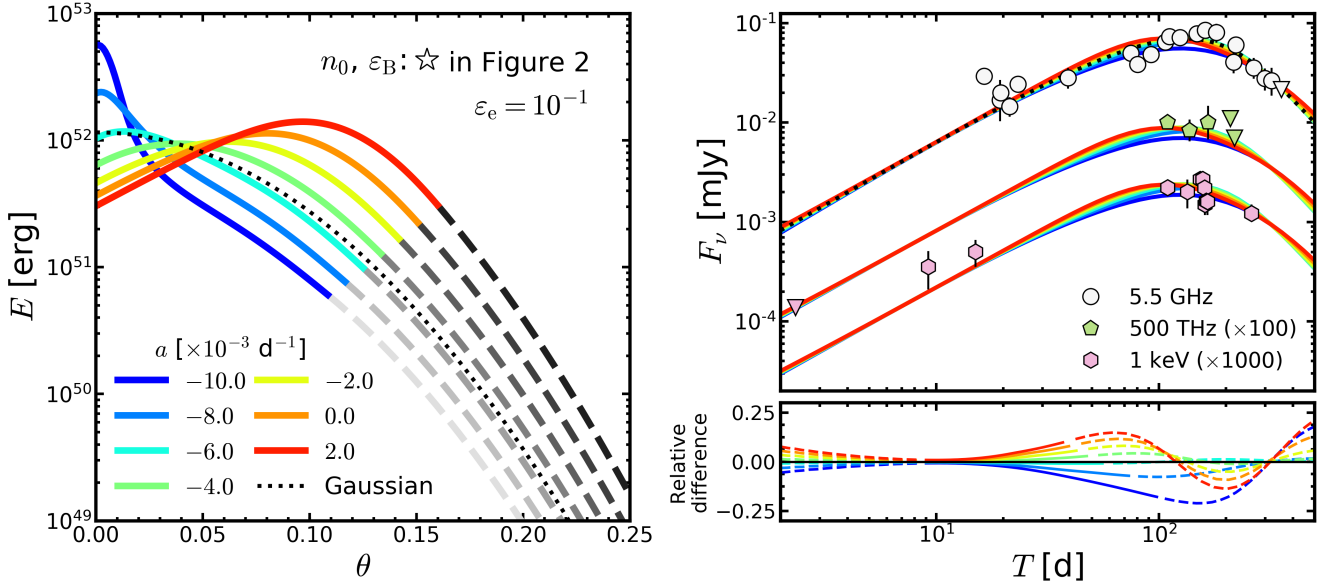


Figure 1. **Left:** Jet structures inversely reconstructed from the radio ($\nu = 5.5$ GHz) light curves with different values of the curvature parameter a . The light curves used for inversion are given by Equation (2) with $-10 \leq a/(10^{-3} \text{ d}^{-1}) \leq 2$, $b = 1.22$, $T_0 = 9$ d, and $F_0 = 5.45 \mu\text{Jy}$. The values of n_0 and ε_B are listed in Table 1 and are also shown by a star-shaped point in Figure 2 for each model, while the other parameter values are fiducial ones: $\varepsilon_e = 10^{-1}$, $\theta_v = 0.387$, $p = 2.17$, and $D = 41$ Mpc. The coloured solid lines show the inversely reconstructed jet structures ($\theta < \Theta(T_0)$) while the gray dashed lines correspond to the jet edge part given by Equation (4) with $\theta_j = 0.61$ ($\theta \geq \Theta(T_0)$), which has to be assumed for inversion. The black dotted line shows the Gaussian given by $E = E_G \exp[-\theta^2/(2\theta_G^2)]$ with $E_G = 1.16 \times 10^{52}$ erg and $\theta_G = 5.90 \times 10^{-2}$. **Top Right:** Light curves forwardly calculated by the reconstructed jets shown in the left panel, which are for radio (5.5 GHz), optical (500 THz), and X-ray (1 keV) from top to bottom for each colour. The black dotted line shows the radio light curve that is generated by the Gaussian jet with (n_0, ε_B) presented by the black star in Figure 2. Also shown for reference are the observed afterglow (points) and upper limits (lower triangles) of GRB 170817A. The data points for radio were taken from Figure 4 in Troja et al. (2019), which uses the data in Hallinan et al. (2017); Lyman et al. (2018); Troja et al. (2018); Margutti et al. (2018); Mooley et al. (2018a); Alexander et al. (2018); Piro et al. (2019). The data points for optical and X-ray were collected from Lyman et al. (2018); Margutti et al. (2018); D’Avanzo et al. (2018); Alexander et al. (2018); Piro et al. (2019). **Bottom Right:** Relative difference of the forwardly calculated light curve with respect to the Gaussian jet light curve, which is defined by $[F_\nu(\text{forward}) - F_\nu(\text{Gaussian})]/F_\nu(\text{Gaussian})$. The solid lines are used for $T_0 \leq T \leq T_f$ while the dashed lines are used for others.

with respect to the light curve for the Gaussian jet. The relative difference increases with T during the time interval that is used for the inversion, $T_0 \leq T \leq T_f$ (solid lines). It reaches ~ 18 per cent at $T_f = 97.9$ d in the case of the spindle jet for $a = -10 \times 10^{-3} \text{ d}^{-1}$. This means that at least the observational accuracy less than ~ 18 per cent is necessary for distinguishing the spindle jet from the Gaussian jet. The light curve for the later phase ($T > T_f$) cannot be used for inversely reconstructing the jet structure, since the jet axis has been already seen to the observer. In the case of the hollow-cone jet for $a = 2 \times 10^{-3} \text{ d}^{-1}$, the relative difference of the light curves reaches ~ 5.8 per cent at $T_f = 37.0$ d. Hence, the observational precision less than 5.8 per cent is necessary to distinguish the hollow-cone jet from the Gaussian jet from the viewpoint of the inverse reconstruction. In the multiband observations of GRB 170817A, the one-sigma errors are comparable or larger than the above demanded values in the rising phase (Makhathini et al. 2020).

3.2 Jet Structure with the Same Shape but with a Different Total Energy

We demonstrate here that the same light curve could be explained by different jet structures that have the same shape but have different total energy, if the ambient number density n_0 and microphysical parameter ε_B are tuned appropriately for each case. We compare the results with those in Section 3.1. It is shown that the total energy of the reconstructed jet is proportional to n_0 , as expected from Section 2.3.

Figure 3 shows the results obtained for the light curves given by Equation (2) with the curvature parameter a in the range of $-10 \leq a/(10^{-3} \text{ d}^{-1}) \leq 2$, which are the same as in Section 3.1, and newly tuned n_0 and ε_B , which are shown in Table 2 and in Figure 2 (round-shaped points). The parameters are tuned by using the degeneracy relation in Section 2.3: n_0 is given by Equation (9) so as to have $E_0 = 2.51 \times 10^{52}$ for the normalization of the jet edge and ε_B is accordingly given by Equation (10) with $\varepsilon_e = \tilde{\varepsilon}_e = 0.1$. As shown in the left panel, the reconstructed jet structure for each light curve has the same shape as the counterpart in Figure 1 but has a different total energy. In fact, the relative difference of the jet shape $f(\theta)$ in Equation (5) is less than

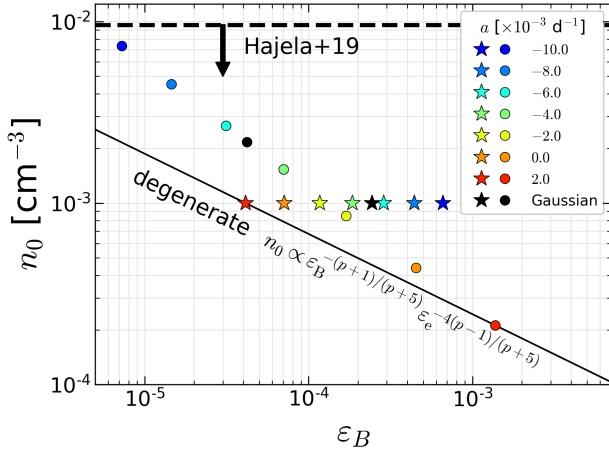


Figure 2. The number density of the ambient matter n_0 and the energy conversion fraction from the shocked matter to the magnetic field ε_B used for the results in Figure 1 (star-shaped points) and those for Figure 3 (round-shaped points). Also shown is the upper limit of n_0 given by Hajela et al. (2019). Note that the pairs of (n_0, ε_B) for the same-coloured star and round points lie on a line that satisfies the degeneracy relation $n_0 \propto \varepsilon_B^{-(p+1)/(p+5)} \varepsilon_e^{-4(p-1)/(p+5)}$ [Equation (6)], as indicated by the black solid line for the red points for example. The pairs (n_0, ε_B) in the degeneracy relation give the jet structures with the same shape but with the total energy that scales with n_0 for a given afterglow light curve.

² The total energy E_{tot} scales with n_0 , since E_{tot}/n_0 for each jet is the same as in Section 3.1 as presented in the rightmost column in Table 2. As a result of the tuning, the total energy E_{tot} is larger for spindle jets than for hollow-cone jets in Figure 3, which is contrast to the jets in Figure 1.

The top right panel of Figure 3 shows the light curves generated by the jets in the left panel. We note that the light curves in Figures 1 and 3 for each a are almost indistinguishable. In fact, the relative difference between the light curves in Figures 1 and 3 is less than 10^{-6} in optical and X-ray. This is a natural consequence from the degeneracy relation.

The above is also true in radio. However the relative difference is relatively large in early phase $T \sim 2$ d as displayed in Figure 4, which shows that the relative difference is ~ 0.1 in the case of the spindle jet for $a = -10 \times 10^{-3} \text{ d}^{-1}$ and the hollow-cone jet for $a = 2 \times 10^{-3} \text{ d}^{-1}$. This is because the degeneracy relation holds only for the frequencies that lies in $\nu'_m \leq \nu' \leq \nu'_c$ (See Appendix C) while $\nu' < \nu'_m$ is realized for $\nu = 5.5$ GHz in a region close to the jet axis when the jet Lorentz factor Γ is still large. The frequency can drop below the synchrotron characteristic frequency due to the different dependencies of ν' and ν'_m on Γ : $\nu' \propto \Gamma \nu$ and $\nu'_m \propto \gamma'_m{}^2 B' \propto \Gamma^3$, where we assumed the observer direction is outside the beaming cone and γ'_m and B' are the minimal Lorentz factor of the accelerated electrons and the magnitude of the magnetic field in the proper frame, respectively.

² The relative difference between the jet structures comes from the numerical errors and the relativistic approximation ($\Gamma \gg 1$) used for deriving the degeneracy relation (See Appendix C). The situation is the same for the relative difference in the light curves.

We can show that ε'_ν increases with n_0 for a frequency below the characteristic frequency, $\nu' < \nu'_m$, as given by Equation (D5). The early emission from the inner region is not significant because of the relativistic debeaming, but it leads to a quantitative difference as shown in Figure 4. The radio light curves obtained here is brighter than those in the previous subsection for $a \leq -4 \times 10^{-3}$ because n_0 is larger as shown in Figure 2. On the other hand, the afterglow becomes dimmer in radio because of smaller n_0 for $a \geq -2 \times 10^{-3}$ than that in Section 3.1. The region with $\nu' < \nu'_m$ shrinks as the shock is decelerated and, hence, the difference between the light curves decreases as time passes.

As demonstrated above, the jet structure is determined from a given light curve except for the energy normalization. It is necessary to fix n_0 , ε_B , and ε_e for determining the energy scale (See Section 2.1 for the uncertainty of θ_v). Early observations with multiple frequencies across the synchrotron break frequency may resolve the degeneracy of the energy scaling.

4 DISCUSSIONS

4.1 Why do the jets with totally different structures generate similar light curve peaks?

We here discuss the result in Section 3.1: Why do the jets with totally different structures generate afterglows with nearly the same peak time and flux, as presented in Figure 1?

To answer the question, we decompose the radio light curve into the contributions from annulus regions on the jet surface, $\theta_n \leq \theta \leq \theta_{n+1}$ with $\theta_n = 0.05n$ ($n = 0, 1, 2, \dots$). Figure 5 shows the decomposition of the light curves generated by three representative jet structures in Figure 1: the spindle jet for the curvature parameter $a = -10 \times 10^{-3} \text{ d}^{-1}$, the Gaussian jet, and the hollow-cone jet for $a = 2 \times 10^{-3} \text{ d}^{-1}$ from top to bottom, respectively. In the case of the spindle jet, the more inner region gradually dominates the light curve as time passes and the most inner region close to the jet axis contributes to the peak flux. This is natural, since the energy of the spindle jet is higher for more inner region. On the other hand, in the case of the hollow-cone jet, the peak of the light curve is dominated by the emission from the middle region of the jet with $0.1 \leq \theta \leq 0.15$ while the emission from the more inner region is sub-dominant. As shown in Figure 1, $E(\theta)$ peaks around $\theta \sim 0.1$ for the hollow-cone jet and the energy at $\theta = 0.1$ is larger than that for the spindle jet. Hence, recalling that the ambient density n_0 is the same, the middle region of the hollow-cone jet becomes visible later than that of the spindle jet. The peak flux is adjusted by tuning ε_B . The hollow-cone jet needs smaller ε_B than the spindle jet to suppress the emission from the middle region. The emission coming from the central region is sub-dominant in the hollow-cone jet simply because the jet energy is lower than in the middle region. In the case of the Gaussian jet (middle panel), which lies between the spindle jet and the hollow-cone jet, the emission from the jet region with $0.05 \leq \theta < 0.1$ produces the peak.

To sum up, the afterglow peaks can be similar even for totally different jet structures, because of the two reasons:

- (i) The light curve peak is generated by the emission from

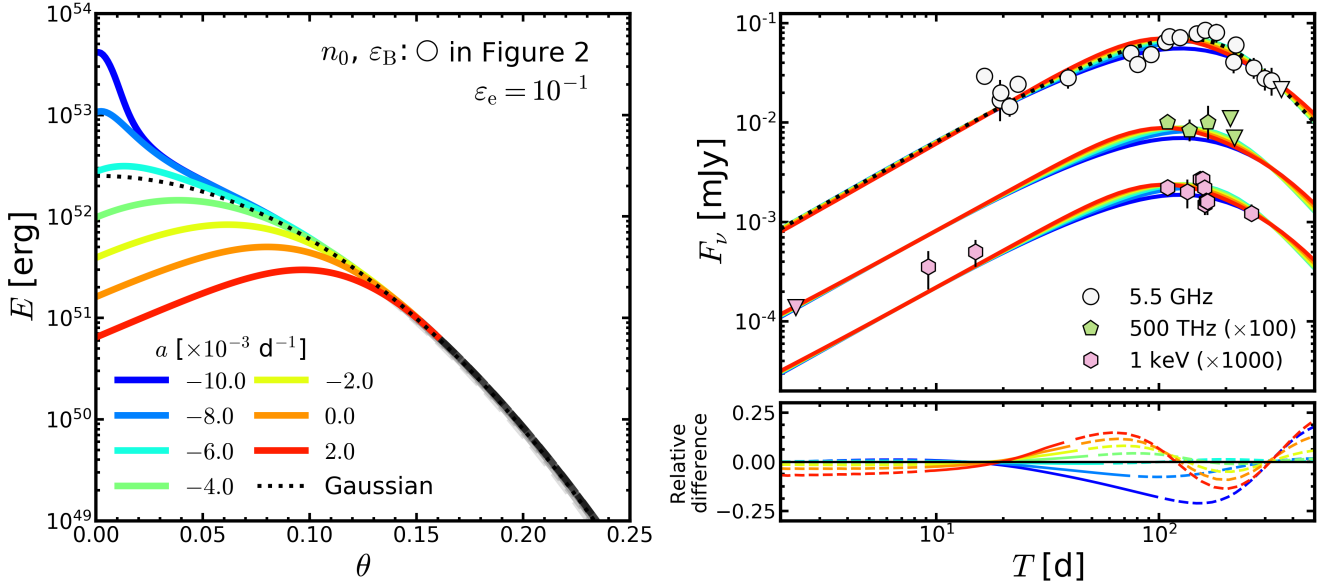


Figure 3. Same as Figure 1 but for n_0 and ε_B that are listed in Table 2 and are also shown by the round-shaped points in Figure 2. The dotted line in the left panel shows the Gaussian given by $E = E_G \exp[-\theta^2/(2\theta_G^2)]$ with $E_G = 2.51 \times 10^{52}$ erg and $\theta_G = 5.90 \times 10^{-2}$. The jet structure reconstructed from each light curve has the same shape as the counterpart in Figure 1 but has a different total energy. The forwardly calculated light curves in optical and X-ray agree well with those in Figure 1 while the radio light curve is slightly (at most 10 per cent) different (See also Figure 4).

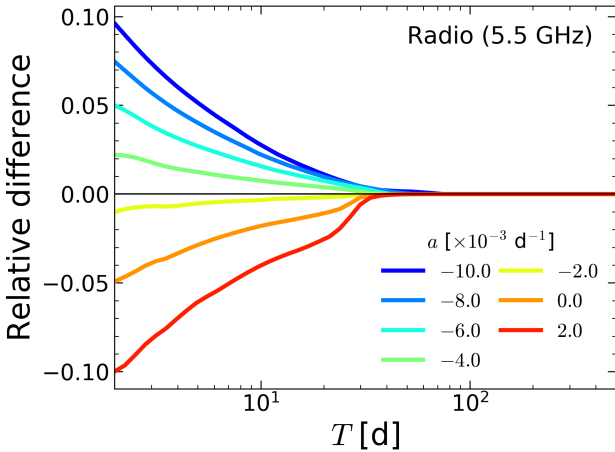


Figure 4. Relative difference of the forwardly calculated radio light curves in Figures 1 and 3 for each a , which is defined by $[F_\nu(\text{Fig. 3}) - F_\nu(\text{Fig. 1})]/F_\nu(\text{Fig. 1})$. The light curves are slightly different because of the different contribution from the region close to the jet axis, where the frequency drops below the synchrotron characteristic frequency in the fluid rest frame, $\nu' < \nu'_m$, for which the emissivity increases with n_0 . As the shock is decelerated, $\nu' > \nu'_m$ is realized in the entire region of the shock and the difference is reduced.

the characteristic position of the jet, which is the energy peak on the middle region in the case of hollow-cone jets while it is the jet axis in the case of spindle jets.

(ii) The emission from the characteristic position is adjustable by tuning the energy scale of the jet (or the num-

ber density n_0) and the energy conversion fraction from the shocked matter to the magnetic field ε_B . The peak time T_p is adjusted by tuning the energy scale: The peak time is advanced/delayed for smaller/larger energy when n_0 is fixed. It is also possible to shift the peak time to an earlier/later time by giving smaller/larger n_0 (Nakar & Piran 2020). The peak flux is adjusted by ε_B . Smaller ε_B reduces the synchrotron flux while larger ε_B enhances the emission.

4.2 Why does the curvature of the light curve slope determine the shape of the jet structure?

As shown in Section 3, different jet structures are reconstructed from light curves with different values of the curvature parameter a , which controls the changing rate of the light curve slope. As shown in TI20, we confirm that the jet structure is mainly determined by a given light curve while the other parameters only quantitatively change the structure. The reason is explained as follows. The slope is determined by how rapidly the inner region of the jet becomes visible. The light curve goes upward with time (i.e., the light curve is convex downward) if the inner region becomes visible earlier. On the other hand, the light curve becomes convex upward if the inner region is seen later. For example, a spindle jet is reconstructed from a convex upward light curve with $a < 0$. This is because the jet inner region is seen late because of the relativistic beaming with the higher jet energy contained around the jet axis. On the other hand, a convex-downward light curve with $a > 0$ reconstructs a hollow-cone jet, because the jet inner region becomes visible earlier.

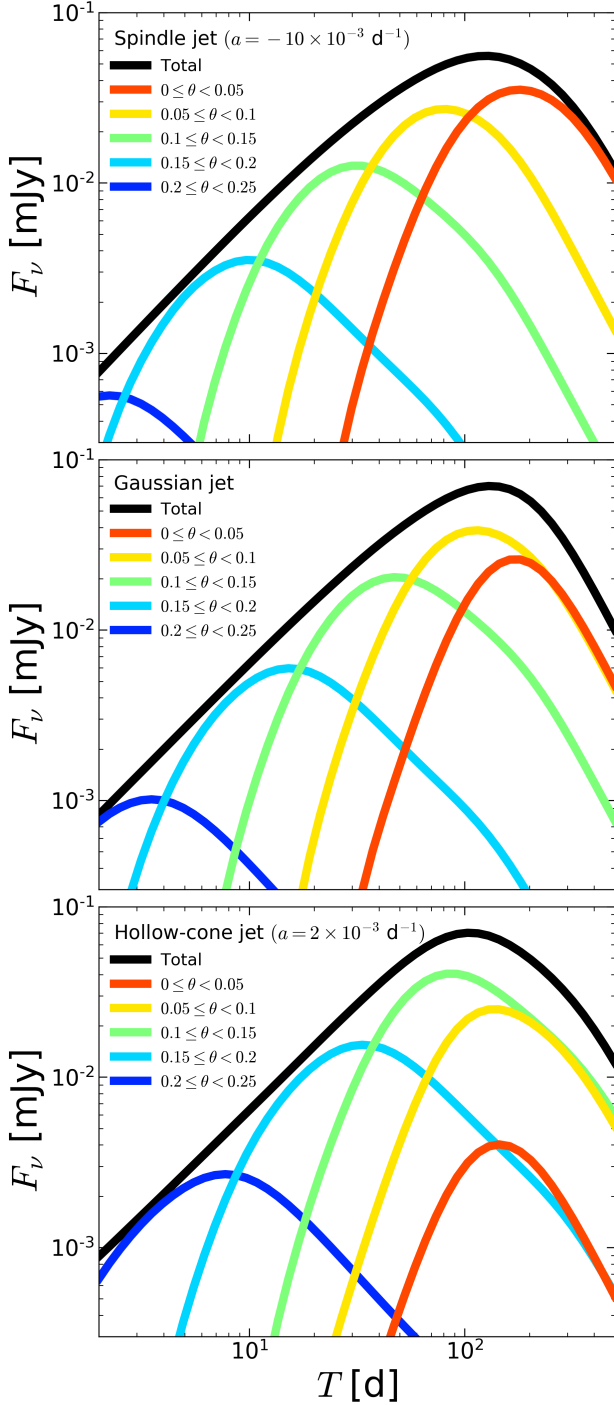


Figure 5. Decomposition of the radio light curve in Figure 1 for the spindle jet obtained for $a = -10 \times 10^{-3} \text{ d}^{-1}$, Gaussian jet, and hollow-cone jet obtained for $a = 2 \times 10^{-3} \text{ d}^{-1}$ from top to bottom, respectively. Each coloured line shows the light curve that is contributed from an annulus area on the jet surface, while the black one shows the total light curve, which is the same as in Figure 1.

5 SUMMARY & CONCLUSIONS

We investigated possible jet structures consistent with the afterglow of GRB 170817A by applying the method of the inverse reconstruction in our previous paper (TI20). We studied how the jet structure depends on the light curve by gradually changing the curvature parameter of the light curve a within the observational errors, which gives convex downward light curves for $a > 0$ and convex upward ones for $a < 0$. We found that hollow-cone jets are reconstructed from light curves with larger a while spindle jets are reconstructed from light curves with smaller a . The structure gradually changes by passing through a Gaussian-like structure as a changes.

In spite of the totally different jet structures, they generate similar light curves, which are consistent with the observed afterglow of GRB 170817A within errors. The light curve peak is produced by the emission from the jet surface where the jet energy peaks. The peak time and the peak flux can be adjusted for each jet structure by tuning the number density of the ambient medium n_0 , the energy conversion fraction from the shocked matter to the magnetic field ϵ_B , and the energy conversion fraction from the shocked matter to the accelerated electrons ϵ_e .

These jet structures are distinguished by precisely observing the rising afterglow with the aid of the inversion method. The precision less than 18 per cent is required in the early phase $T \leq 98 \text{ d}$ to distinguish the spindle jet from the Gaussian jet while less than 6 per cent is necessary in $T \leq 37 \text{ d}$ to distinguish the hollow-cone jet from the Gaussian jet as indicated by Figure 1. In the case of GRB 170817A, the observational one-sigma errors are comparable or larger in the rising phase (Makhathini et al. 2020). Hence, more precise observations are necessary for determining jet structures from the inverse reconstruction. Such observations would be possible for future events in denser environment, for which afterglow light curves become brighter (Gottlieb et al. 2019; Duque et al. 2020; O’Connor et al. 2020). In the same reason, future events with a smaller viewing angle are also preferable, whereas the viewing angle has to be large enough so that the jet structure is reflected into observed light curves.

We found that the total energy of the jet can be tuned without changing the jet shape by using a different appropriate combination of the afterglow parameters (n_0 , ϵ_B , and ϵ_e). We discovered that the degenerate combination is given by Equation (6), which is applicable to any jet structure as demonstrated in this paper. We showed that the total energy is proportional to n_0 . We also note that the viewing angle is another cause of the degeneracy, where a larger viewing angle leads to a wider jet shape (Nakar & Piran 2020; Takahashi & Ioka 2020). In order to break the degeneracy of the parameters, multi-frequency observations across the synchrotron break or cooling frequency would be important. Here, future events in denser environment are preferred again, since the spectral break shifts to the observed frequency. Indeed, the synchrotron frequency and cooling frequency respectively satisfy $\nu_m \propto E^{1/2} \epsilon_B^{1/2} \epsilon_e^{-2} T^{-3/2}$ and $\nu_c \propto n_0^{-1} E^{-1/2} \epsilon_B^{-3/2} T^{-1/2}$ (Sari et al. 1998). Increasing n_0 shifts ν_m to a larger frequency and ν_c to a smaller frequency, since the shock decelerates earlier and more inner

region with larger E is seen for larger n_0 when ε_B , ε_e , and T are fixed.³

As demonstrated in this paper, there is a large variety of possible jet structures for GRB 170817A consistent with the afterglow observations within errors. Since the inner jet structure is solely determined by the curvature of the light curve, qualitatively the same diversity should emerge even for the power-law edge as demonstrated in [TI20](#). There are several possible ways to form a hollow-cone jet in GRBs: the Blandford-Znajek mechanism ([Blandford & Znajek 1977](#); [McKinney 2006](#); [Tchekhovskoy et al. 2008](#)), the interaction between the jet and the ambient medium during the propagation through the ejecta or at the jet breakout ([Zhang et al. 2003](#); [Mizuta & Ioka 2013](#)), and jet precession ([McKinney 2013](#); [Kawaguchi et al. 2015](#); [Huang et al. 2019](#)), for example. It would be worth noting that hollow-cone jets are found in magnetohydrodynamical simulations (e.g., [Kathirgamaraju et al. 2019](#); [Nathanail et al. 2020](#)), whereas [Gottlieb et al. \(2020\)](#) recently found jet structures consistent with a classical power-law jet in their hydrodynamical simulations, which results from fluid instabilities at the jet-cocoon interface. It is also worth noting that [Salafia et al. \(2020\)](#) invoked a two-component jet similar to the spindle jet found in this paper that explains the luminosity function of the short GRBs, although they used a rather simple analytic model (c.f. [Hamidani et al. 2019](#)). Anyway, the jet structure of short GRBs is still under debate in theoretical studies. High cadence and accuracy are necessary for the observations in the rising phase of the afterglow to determine the GRB jet structure.

ACKNOWLEDGEMENTS

We thank Bing Zhang, Hamid Hamidani, Koutarou Kyutoku, Tomoki Wada, and Wataru Ishizaki for useful discussion. We acknowledge the YITP workshops YITP-W-19-04, YITP-W-18-12, and YITP-W-18-11. This work is supported by JSPS Grants-in-Aid for Scientific Research 17H06362 (KT, KI) and 20H01904, 20H01901, 20H00158, 18H01213, 18H01215, 17H06357, 17H06131 (KI).

DATA AVAILABILITY

The data underlying this article will be shared on reasonable request to the corresponding author.

REFERENCES

Abbott B. P. et al., 2017a, PRL, 119, 161101
 Abbott B. P. et al., 2017b, ApJL, 848, 12
 Abbott B. P. et al., 2017c, ApJL, 848, 13
 Alexander K. D. et al., 2018, ApJL, 863, 18
 Aloy M. A., Janka H.-T., Müller E., 2005, A&A, 436, 273
 Beniamini P., Petropoulou M., Duran R. B., Giannios D., 2019, MNRAS, 483, 840

³ The situation is the same even for hollow-cone jets as long as we consider the rising phase of the afterglow, since the light curve before the peak is generated by the emission from the region outside the energy peak as discussed in Section 4.1.

Beniamini P., Granot J., Gill R., 2020, MNRAS, 493, 3521
 Blandford R. D., McKee C. F., 1976, Phys. Fluids, 19(8), 1130
 Blandford R. D., Znajek R. L., 1977, MNRAS, 179, 433
 Cantiello M. et al., 2018, ApJL, 854, 31
 D’Avanzo P. et al., 2018, A&A, 613, L1
 Duffell P. C., Quataert E., MacFadyen A. I., 2015, ApJ, 813, 64
 Duque R., Beniamini P., Daigne F., Mochkovitch R., 2020, A&A, 639, A15
 Fong W. et al., 2019, ApJL, 883, L1
 Geng J.-J., Zhang B., Kölligan A., Kuiper R., Huang Y.-F., 2019, ApJL, 877, L40
 Ghirlanda G. et al., 2019, Science, 363, 968
 Gill R., Granot J., 2018, MNRAS, 491, 5815
 Gill R., Granot J., De Colle F., Urrutia G., 2019, ApJ, 883, 15
 Goldstein A. et al., 2017, ApJL, 848, 14
 Gottlieb O., Nakar E., Piran T., 2019, MNRAS, 488, 2405
 Gottlieb O., Nakar E., Bromberg O., 2020, arXiv: 2006.02466
 Granot J., Kumar P., 2003, ApJ, 591, 1086
 Granot J., Piran T., Sari R., 1999, ApJ, 513, 679
 Hajela A. et al., 2019, ApJL, 886, L17
 Hallinan G. et al., 2017, Science, 358, 1579
 Hamidani H., Kiuchi K., Ioka K., 2019, MNRAS, 491, 3192
 Hjorth J. et al., 2017, ApJL, 848, 31
 Huang B.-Q., Lin D.-B., Liu T., Ren J., Wang X.-G., Liu H.-B., Liang E.-W., 2019, MNRAS, 487, 3214
 Ioka K., Nakamura T., 2018, PTEP, 043E02
 Ioka K., Nakamura T., 2019, MNRAS, 487, 4884
 Kathirgamaraju A., Duran R. B., Giannios D., 2018, MNRAS, 473, L121
 Kathirgamaraju A., Tchekhovskoy A., Giannios D., Duran R. B., 2019, MNRAS, 484, L98
 Kawaguchi K., Kyutoku K., Nakano H., Okawa H., Shibata M., Taniguchi K., 2015, PRD, 92, 024014
 Kumar P., Granot J., 2003, ApJ, 591, 1075
 Kumar P., Zhang B., 2015, Phys. Rep., 561, 1
 Lamb G. P., Kobayashi S., 2018, MNRAS, 478, 733
 Lamb G. P. et al., 2019, ApJL, 870, 15
 Lazzati D., López-Cámara D., Cantiello M., Morsony B. J., Perna R., Workman J. C., 2017, ApJL, 848, L6
 Lyman J. D. et al., 2018, NatAs, 2, 751
 Makhathini S. et al., 2020, arXiv: 2006.02382
 Margutti R. et al., 2018, ApJL, 856, 18
 McKinney J. C., 2006, MNRAS, 368, 1561
 McKinney J. C., Tchekhovskoy A., Blandford R. D., 2013, Science, 339, 49
 Mészáros P., Rees M. J., Wijers R. A. M. J., 1998, ApJ, 499, 301
 Mizuta A., Ioka K., 2013, ApJ, 777, 162
 Mooley K. P. et al., 2018a, Nature, 554, 207
 Mooley K. P. et al., 2018b, Nature, 561, 355
 Mooley K. P. et al., 2018c, ApJL, 868, 11
 Mulguita-Berthier A. et al., 2017, ApJL, 868, L34
 Nakar E., Piran T., 2020, arXiv:2005.01754
 Nagakura H., Hotokezaka K., Sekiguchi Y., Shibata M., Ioka K., 2014, ApJL, 784, 28
 Nathanail A., Gill R., Porth O., Fromm C. M., Rezzolla L., 2020, arXiv:2003.03597
 O’Connor B., Beniamini P., Kouveliotou C., 2020, MNRAS, 495, 4782
 Piro L. et al., 2019, MNRAS, 483, 1912
 Resmi L. et al., 2018, ApJ, 867, 57
 Rossi E., Lazzati D., Rees M. J., 2002, MNRAS, 332, 945
 Rossi E., Lazzati D., Salmonson J. D., Ghisellini G., 2004, MNRAS, 354, 86
 Ryan G., van Eerten H., Piro L., Troja E., 2020, ApJ, 896, 166
 Salafia O. S., Barbieri C., Ascenzi S., Toffano M., 2020, A&A, 636, 105
 Sari R., Piran T., Narayan R., 1998, ApJL, 497, 17
 Savchenko V. et al., 2017, ApJL, 848, 15

- Sedov L. I., 1959, *Similarity and Dimensional Methods in Mechanics*. Academic Press, New York
- Shull J. L., Smith B. D., Danforth C. W., 2012, *ApJ*, 759, 23
- Sironi L., Spitkovsky A., 2011, *ApJ*, 726, 75
- Takahashi K., Ioka K., 2020, *MNRAS*, in press (arXiv:1912.01871)
- Taylor G., 1950, *Proc. R. Soc. A*, 201, 159
- Tchekhovskoy A., McKinney J. C., Narayan R., 2008, *MNRAS*, 388, 551
- Troja E. et al., 2018, *MNRAS*, 478, L18
- Troja E. et al., 2019, *MNRAS*, 489, 1919
- Troja E. et al., 2020, arXiv: 2006.01150
- van Eerten H. J., MacFadyen A. I., 2012, *ApJ*, 751, 155
- van Eerten H., Zhang G., MacFadyen A., 2010, *ApJ*, 722, 235
- Xie X., Zrake J., MacFadyen A., 2018, *ApJ*, 863, 58
- Zhang W., MacFadyen A., 2009, *ApJ*, 698, 1261
- Zhang B., Mészáros P., 2002, *ApJ*, 571, 876
- Zhang W., Woosley S. E., MacFadyen A. I., 2003, *ApJ*, 586, 356

APPENDIX A: REVIEW OF THE INVERSION FORMULA

Based on [TI20](#), we give a brief review of our inversion formula, Equation (1), which is obtained by differentiating Equation (A1) with respect to T and using Equation (A4). See Section 2.1 for the basic picture of the afterglow model.

The observed afterglow is contributed only from a limited region of the jet surface around the line of sight of the off-axis observer due to relativistic beaming effects. Hence, the observed flux $F_\nu(T)$, where ν and T are respectively the observed frequency and the observer time, is approximately given by integrating the synchrotron emission in a limited polar angle region between $\Theta(T)$ and θ_j :

$$F_\nu(T) \sim \int_{\Theta(T)}^{\theta_j} d\theta K(T, \theta, E(\theta)), \quad (\text{A1})$$

where θ_j is a given jet truncation angle. $\Theta(T)$ is the inner-side edge of the emission site that mainly contributes to the observed afterglow for each time, which is defined by

$$\Theta = \theta_v - \frac{f_b}{\Gamma} \sim \theta_v - 4f_b \left[\frac{\pi n_0 m_p c^5}{17(1 + 8f_b^2)^3} \right]^{1/8} E^{-1/8} (\Theta) T^{3/8}, \quad (\text{A2})$$

where m_p and c are the proton mass and the speed of light, respectively. f_b is the size of the emission region measured by $1/\Gamma$, and we adopt $f_b = 7$ throughout the paper as in [TI20](#). The inversion process is finished when $\Theta(T)$ becomes zero, which takes place at T_f given by

$$T_f = 60.2 \text{ day} \left(\frac{E_{\text{axis}}}{10^{52} \text{ erg}} \right)^{1/3} \left(\frac{n_0}{10^{-3} \text{ cm}^{-3}} \right)^{-1/3} \left(\frac{\theta_v}{0.4} \right)^{8/3}, \quad (\text{A3})$$

where $E_{\text{axis}} = E(0)$. The time derivative of Θ is obtained by differentiating Equation (A2) with respect to T as follows:

$$\frac{d\Theta}{dT} = -\frac{3(\theta_v - \Theta)}{8T} \left(1 - \frac{\theta_v - \Theta}{8} \frac{d \ln E}{d\Theta} \right)^{-1}. \quad (\text{A4})$$

In Equation (A1), $K(T, \Theta, E(\Theta))$ is given by

$$K(T, \theta, E(\theta)) = \frac{1}{4\pi D^2} \int_0^{2\pi} d\phi \left. \frac{\sin \theta R_s^3 \epsilon'_{\nu'}}{12\Gamma^4 (1 - \beta_{\text{sh}} \mu)(1 - \beta \mu)^2} \right|_{t=t_s}, \quad (\text{A5})$$

which integrates the synchrotron emissivity $\epsilon'_{\nu'}$ on a thin

annulus. In the above equation, ϕ is the azimuthal angle around the jet axis and

$$\mu = \sin \theta \sin \theta_v \cos \phi + \cos \theta \cos \theta_v \quad (\text{A6})$$

is the cosine of the angle spanned by the radial vector and the line of sight for the observer located at $\phi = 0$. Γ and β are the Lorentz factor and the normalized speed of shocked fluid while those with the subscript ‘sh’ are of the shock wave, which satisfy

$$\Gamma_{\text{sh}}^2 \beta_{\text{sh}}^2 = C_{\text{BM}}^2 t^{-3}, \quad (\text{A7})$$

$$\Gamma^2 \beta^2 = \frac{1}{2} C_{\text{BM}}^2 t^{-3}, \quad (\text{A8})$$

$$C_{\text{BM}} = \sqrt{\frac{17E}{8\pi n_0 m_p c^5}}, \quad (\text{A9})$$

with t being the laboratory time elapsed from the explosion that launches the jet at the origin. Equations (A7) and (A8) reduce to a self-similar solution of [Blandford & McKee \(1976\)](#) in the ultra-relativistic limit ($\beta = \beta_{\text{sh}} = 1$). These factors, β and β_{sh} , are introduced to ensure $\Gamma_{\text{sh}} > 1$ and $\Gamma > 1$ for any t , while they do not affect the observed flux, which is contributed from the relativistic region during the inversion process. R_s in Equation (A5) is the shock radius given by integrating $c\beta_{\text{sh}}$ with respect to t :

$$R_s(t) = {}_2F_1 \left(\frac{1}{3}, \frac{1}{2}, \frac{4}{3}; -\frac{t^3}{C_{\text{BM}}^2} \right) ct, \quad (\text{A10})$$

where ${}_2F_1(\dots)$ is the Gauss’s hypergeometric function. The synchrotron emissivity $\epsilon'_{\nu'}$ in Equation (A5) is given by

$$\epsilon'_{\nu'} = \epsilon'_{\nu',p} \left(\frac{\nu'}{\nu'_m} \right)^{-(p-1)/2}, \quad (\text{A11})$$

where we assume the observed frequency in the fluid rest frame

$$\nu' = \Gamma(1 - \beta\mu)\nu \quad (\text{A12})$$

lies between the characteristic frequency ν'_m and the cooling frequency ν'_c as $\nu'_m < \nu' < \nu'_c$, which is appropriate in the case of GRB 170817A. The characteristic frequency and the corresponding emissivity are given by ([Granot et al. 1999](#); [van Eerten et al. 2010](#))

$$\nu'_m = \frac{3}{16} \left[\epsilon_e \frac{p-2}{p-1} \frac{m_p}{m_e} (\Gamma-1) \right]^2 \frac{q_e B'}{m_e c}, \quad (\text{A13})$$

$$\epsilon'_{\nu',p} = 0.88 \cdot \frac{256}{27} \frac{p-1}{3p-1} \frac{q_e^3}{m_e c^2} n' B', \quad (\text{A14})$$

where q_e is the elementary charge and m_e is the electron mass. n' and B' denote the number density and magnetic field measured at the fluid rest frame, which are given by

$$n' = 4\Gamma n_0, \quad (\text{A15})$$

$$B' = \sqrt{32\pi \epsilon_B n_0 \Gamma (\Gamma-1) m_p c^2}. \quad (\text{A16})$$

t_s in Equation (A5) is the laboratory time that emits the photons arriving at the observer at T , which is given as the solution of the following equation:

$$t_s = T + \frac{\mu R_s(t_s)}{c}, \quad (\text{A17})$$

where we choose $T = 0$ as the arrival time of a photon emitted

at the origin at $t = 0$. We employ an approximated analytic solution of Equation (A17) for t_s , which is obtained in the relativistic limit (See appendix A in TI20).

APPENDIX B: CONSTRAINTS ON THE JET EDGE STRUCTURE

We constrain the jet edge structure as follows. Suppose that a light curve starts at an initial time T_0 and the parameters $\{n_0, \varepsilon_B, \varepsilon_e, \theta_v, p, D\}$ and the jet truncation angle θ_j are given. Then, the jet edge structure $E(\theta)$ ($\Theta(T_0) < \theta \leq \theta_j$) should satisfy Equation (A1) at the initial time T_0 :

$$F_\nu(T_0) = \int_{\Theta(T_0)}^{\theta_j} d\theta K(T_0, \theta, E(\theta)). \quad (\text{B1})$$

In addition, if the light curve is smooth at T_0 , the jet edge structure also satisfies the first derivative of Equation (B1) at T_0 :

$$\begin{aligned} \frac{dF_\nu}{dT}(T_0) &= \frac{d\Theta}{dT}(T_0) K(T_0, \Theta(T_0), E(\Theta_0)) \\ &+ \int_{\Theta(T_0)}^{\theta_j} d\theta \frac{dK}{dT}(T_0, \theta, E(\theta)). \end{aligned} \quad (\text{B2})$$

In the same manner, higher derivatives of the light curve at the initial time give constraints on $E(\theta)$ ($\Theta(T_0) < \theta \leq \theta_j$) in principle, whereas the higher derivatives are difficult to obtain from observations. In this paper, we use only Equations (B1) and (B2). Since we assume a Gaussian edge given by Equation (4), these equations determine the normalization E_0 and the standard deviation θ_c of the jet edge. See TI20 for the prescription for the power-law edge.

APPENDIX C: DERIVATION OF THE DEGENERACY RELATION

Let us derive the degeneracy relation described in Section 2.3. That is, we show that for the combinations of $(n_0, \varepsilon_B, \varepsilon_e)$ in Equation (6), the jet structures reconstructed from a given light curve have the same shape $f(\theta)$ but the energy E_{axis} scales with n_0 [Equation (7)], where we decompose a jet structure to the shape and normalization as given by Equation (5).

The inversion formula, Equation (1), is equivalent to Equation (A1). In the relativistic limit ($\Gamma \gg 1$), which is a good approximation unless the shock is entirely decelerated to non-relativistic speeds, Equation (A1) reduces to

$$F_\nu(T) \propto [E_{\text{axis}} f(\Theta(T))]^{(p+3)/4} n_0^{1/2} \varepsilon_B^{(p+1)/4} \varepsilon_e^{p-1} T^{-3(p-1)/4}. \quad (\text{C1})$$

Here, we used $\Gamma \propto E^{1/2} n_0^{-1/2} t^{-3/2}$ [Equation (A8)] and $t \sim T/(1 - \beta\mu) \sim \Gamma^2 T$ [Equation (A17)], which lead to $\Gamma \propto E^{1/8} n_0^{-1/8} T^{-3/8}$. We also employed $R_s \sim c\beta t \propto \Gamma^2 T$ [Equation (A10)], $\varepsilon'_{\nu, p} \propto n_0^{(p+5)/4} \varepsilon_B^{(p+1)/4} \varepsilon_e^{p-1} \Gamma^{p+1} (1 - \beta\mu)^{-(p-1)/2} \propto n_0^{(p+5)/4} \varepsilon_B^{(p+1)/4} \varepsilon_e^{p-1} \Gamma^{2p}$ [Equation (A11)], and $\Delta\Omega \propto \Gamma^{-2}$, where $\Delta\Omega$ is the solid angle of the luminous region that

dominates the integral. $\Theta(T)$ in Equation (C1) obeys Equation (A2). Equation (A2) can be also written by

$$\Theta(T) = \begin{cases} \theta_v - A \left[\frac{E_{\text{axis}} f(\Theta(T))}{n_0} \right]^{-1/8} T^{3/8} & (T \leq T_f) \\ 0 & (T > T_f) \end{cases}, \quad (\text{C2})$$

where A is a constant. Eliminating $E_{\text{axis}} f(\Theta(T))$ from Equation (C1) with Equation (C2), we obtain

$$F_\nu(T) \propto [\theta_v - \Theta(T)]^{-2(p+3)} n_0^{(p+5)/4} \varepsilon_B^{(p+1)/4} \varepsilon_e^{p-1} T^3. \quad (\text{C3})$$

Since a light curve $F_\nu(T)$ and the viewing angle θ_v are supposed to be fixed, the following things should hold: First, $n_0^{(p+5)/4} \varepsilon_B^{(p+1)/4} \varepsilon_e^{p-1}$ is a constant; Second, $\Theta(T)$ is a fixed function of T . The former is equivalent to the degeneracy relation, Equation (6). The latter and Equation (C2) lead to $E_{\text{axis}} \propto n_0$, Equation (7), and that $f(\theta)$ is a fixed function. Conversely, if $f(\theta)$ is fixed and Equations (6) and (7) are satisfied, $\Theta(T)$ is an invariant and hence $F_\nu(T)$ is also an invariant.

Note that we assumed the synchrotron emissivity is expressed by Equation (A11) in the above. Hence, the degeneracy relation holds only for the frequencies in $\nu'_m \leq \nu' \leq \nu'_c$.

APPENDIX D: SYNCHROTRON EMISSIVITY FOR $\nu' < \nu'_m$

We here argue the synchrotron emissivity $\varepsilon'_{\nu'}$ for $\nu' < \nu'_m$ in the slow cooling case, which is used for the discussion in Section 3.2. We assume Equations (6) and (7) and use the relativistic limit ($\Gamma \gg 1$). For a fixed angular coordinate (θ, ϕ) on the jet surface, Equations (A12) and (A13) lead to

$$\frac{\nu'}{\nu'_m} \propto \Gamma^{-2} n_0^{-1/2} \varepsilon_B^{-1/2} \varepsilon_e^{-2}. \quad (\text{D1})$$

The Lorentz factor given by Equation (A8) obeys the following proportionality for a fixed (θ, ϕ) :

$$\Gamma \propto E^{1/2} n_0^{-1/2} T^{-3/2}, \quad (\text{D2})$$

where we used $t \sim T/(1 - \mu\beta) \propto T$ for fixed μ . Substituting Equations (6), (7), and (D1) to Equation (D2), we obtain

$$\frac{\nu'}{\nu'_m} \propto n_0^{2/(p+1)} \varepsilon_e^{-4/(p+1)} T^3. \quad (\text{D3})$$

In the same manner, we obtain the following equation from Equations (6), (7), (A14), and (D2):

$$\varepsilon'_{\nu', p} \propto n_0^{(p-1)/(p+1)} \varepsilon_e^{-2(p-1)/(p+1)} T^{-3}. \quad (\text{D4})$$

Taking into account that the power-law index for $\nu' < \nu'_m$ is $1/3$ in the case of the slow cooling (Sari et al. 1998), we obtain the following equation from Equations (D3) and (D4):

$$\varepsilon'_{\nu'} \propto n_0^{(3p-1)/[3(p+1)]} \varepsilon_e^{2(3p-1)/[3(p+1)]} T^{-2} (\nu' < \nu'_m). \quad (\text{D5})$$

Thus, if $p > 1/3$, the synchrotron emissivity decreases for smaller n_0 and ε_e for the frequencies below the characteristic frequency, $\nu' < \nu'_m$.

This paper has been typeset from a $\text{\TeX}/\text{\LaTeX}$ file prepared by the author.